Journal of Alloys and Compounds 1044 (2025) 184503

Contents lists available at ScienceDirect

Journal of Alloys and Compounds

journal homepage: www.elsevier.com/locate/jalcom

Microstructure and high-temperature mechanical performance of industrial-scale titanium and chromium beryllides for fusion applications

Ramil Gaisin [a,*], Rolf Rolli [a], Mikhail Podoinikov [b], Viacheslav Kuksenko [c], Klaus Seemann [a], Thomas Bergfeldt [a], Vladimir Chakin [a], Pavel Vladimirov [a]

[a] Karlsruhe Institute of Technology, Hermann-von-Helmholtz-Platz 1, Eggenstein-Leopoldshafen 76344, Germany
[b] Ulba Metallurgical Plant, Abay Avenue 102, Ust-Kamenogorsk 070005, Kazakhstan
[c] United Kingdom Atomic Energy Authority, Culham Science Centre, Abingdon, Oxfordshire OX14 3DB, United Kingdom

ARTICLE INFO

Keywords:
Beryllides
Neutron multiplier material
Mechanical properties
DEMO

ABSTRACT

The development of materials for the breeding blanket of future fusion devices requires a combination of high-temperature strength, radiation resistance, and compatibility with other materials. While beryllides have long been considered as neutron multipliers due to their favorable nuclear properties, their potential structural role has remained largely overlooked. These materials form an exotic class of beryllium-based intermetallics that may offer advantages in both neutronics and mechanical performance. We report the first comprehensive microstructural and mechanical characterization of full-scale $TiBe_{12}$ and $CrBe_{12}$ blocks fabricated by industrial vacuum hot pressing. $TiBe_{12}$ shows a fine-grained (≈7 μm) structure with ≈ 7 % free beryllium and frequent twin boundaries, while $CrBe_{12}$ has coarser grains (≈40 μm) and < 2 % beryllium. Both compounds exhibit high microhardness (>1000 HV) and strong room-temperature compressive strength (2030 MPa for $TiBe_{12}$; 1750 MPa for $CrBe_{12}$). Nanoindentation confirmed hardness values of 13.6–14.5 GPa and elastic moduli of 285 GPa ($TiBe_{12}$) and 304 GPa ($CrBe_{12}$). They retain strength at 1000°C (740 MPa and 460 MPa, respectively) and develop ductility above 850°C, with up to 20 % deformation at 1200°C. In three-point bending, $TiBe_{12}$ reaches 540 MPa at 800°C, outperforming $CrBe_{12}$ and many other materials. The results are compared with available data on $NbBe_{12}$ and Ta_2Be_{17}, as well as with conventional high-temperature materials. Given that only very limited mechanical information exists for beryllides, this study substantially expands the database for this exotic class of compounds. In particular, the identification of twinning in $TiBe_{12}$ and the detailed comparison of strength, hardness, and elastic moduli provide new insights into their deformation behavior. Overall, the findings highlight the potential of $TiBe_{12}$ and $CrBe_{12}$ to bridge functional and structural roles, supporting their application not only in fusion blankets but also in aerospace, fission, and other extreme environments.

1. Introduction

Ensuring a sustainable tritium supply is a fundamental challenge for the realization of future fusion power plants. For instance, the EU DEMO reactor, operating at 2 GW of fusion power, is expected to consume approximately 111 kg of tritium per year [1], while current global production remains limited to just a few kilograms annually [2]. Overcoming this limitation requires the implementation of advanced breeding blanket systems capable of efficient tritium generation, fusion energy conversion, and radiation shielding. A key component of these systems is the neutron multiplier material (NMM), which supplies the tritium breeder with a sufficient flux of moderated neutrons, while also contributing to the blanket's other key functions. Beryllium and lead have been the primary candidates for this role [3] both suffer from significant limitations related to safety, activation, and compatibility with high-temperature fusion environments. This has prompted a search for more advanced materials that retain the desired neutronic properties while offering improved engineering performance.

Beryllium-based intermetallic compounds (beryllides) have emerged as a promising alternative, combining favorable nuclear characteristics with high thermal stability and reduced irradiation-induced degradation. In particular, the compounds $TiBe_{12}$ and $CrBe_{12}$ offer a unique balance of low activation, chemical stability, and high-temperature strength. These properties not only make them attractive for fusion

* Corresponding author.
E-mail address: ramil.gaisin@kit.edu (R. Gaisin).

https://doi.org/10.1016/j.jallcom.2025.184503
Received 29 July 2025; Received in revised form 30 September 2025; Accepted 18 October 2025
Available online 20 October 2025

blanket applications, but also open opportunities for cross-sectoral knowledge transfer, including their potential use in fission reactors, accelerator-driven systems, and high-performance aerospace and propulsion components, where lightweight and heat-resistant materials are critical.

In this work, we report the first detailed microstructural and mechanical characterization of full-sized $TiBe_{12}$ and $CrBe_{12}$ blocks, produced through an industrial-scale fabrication route. Our findings reveal a combination of properties rarely observed in conventional materials, highlighting their potential as multifunctional candidates for both fusion applications and broader technological domains.

2. Materials and experimental techniques

Extensive research on various beryllides was conducted at KIT, leading to the development of an industrial-scale fabrication process in collaboration with the Ulba Metallurgical Plant (UMP) in Ust-Kamenogorsk, Kazakhstan (UMP) [4–6]. The synthesis of the titanium and chromium beryllides starts with the use of pure beryllium, titanium and chromium powders as starting materials. These powders were blended in stoichiometric proportions with a slight excess of beryllium. After the vacuum annealing, performed with the aim of initiating beryllide formation, the resulting materials were subjected to a grinding process into powders, which were further processed using vacuum hot pressing (VHP). The VHP process is carried out in graphite molds, maintaining a temperature range of 0.7–0.8 times the melting point of the corresponding beryllide compound. The specific details of the VHP process remain confidential and will not be disclosed.

After obtaining large beryllide blanks, electrical discharge machining (EDM) was used for further processing. In line with the HCPB design, beryllide blocks are meant to fit the space between steel pins, which contain lithium ceramic pebbles (Fig. 1). This can be done either with hexagonal shaped blocks with a hole in the middle (Fig. 1 left) or with complex shaped blocks (Fig. 1 right). When assembled, the complex-shaped blocks form a hexagonal grid. The grid has holes for inserting steel pins filled with lithium ceramic pebbles. It was decided to produce titanium beryllide in the form of a hexagonal prism, and chromium beryllide in the form of a complex-shaped prism according to an alternative design.

Microstructural studies were performed using a Zeiss Merlin scanning electron microscope (SEM) operated in backscattered electron (BSE) mode. Electron backscatter diffraction (EBSD) was used to build surface normal-projected inverse pole figure (IPF-Z) orientation maps. The black and white lines on the maps indicate high- and low-angle grain boundaries, respectively, while silver lines correspond to twin boundaries. In addition, transmission Kikuchi diffraction (TKD) was employed for $TiBe_{12}$ using thin lamellae prepared for transmission under a tilt angle of 20°. TKD provides higher spatial resolution compared to conventional EBSD and was specifically applied to reveal twin boundaries that could not be clearly resolved at larger EBSD step sizes. TKD was not performed on $CrBe_{12}$, since no twins were observed in this material. Chemical composition of beryllides was analyzed with inductively coupled plasma optical emission spectrometry method (ICP-OES). Microhardness was measured on a Zwick Roell Indentec ZHμ tester using indentation force of 500 gf. Density was measured by the hydrostatic weighing in C14H30 liquid medium (Mettler Toledo MS303TS). X-ray diffraction (XRD) was performed using Cu-$K_{\alpha 1/2}$ radiation to determine the phase composition.

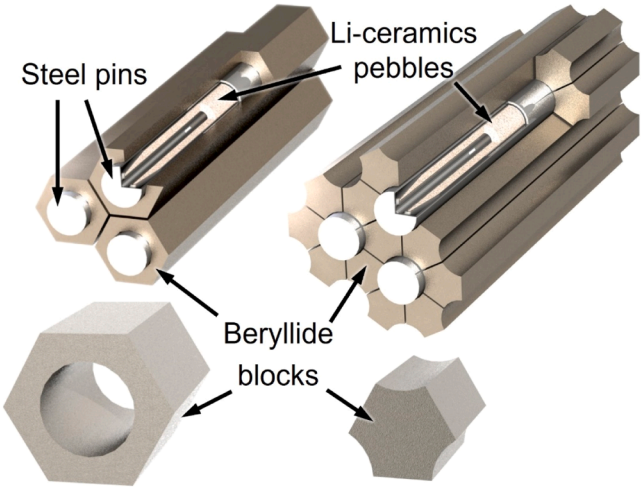

Fig. 1. Variants of filling the space in the blanket between steel pins filled with lithium ceramic pebbles: on the left – blocks of hexagonal-shaped beryllides with an internal hole, and on the right – blocks of complex shape without a hole [7,8].

Indentations were conducted using a Keysight G200 nanoindentation system with a diamond pyramid Berkovich tip using the continuous stiffness measurement (CSM) technique [18] with a 42 Hz and 2 nm oscillation. CSM technique has been selected as it provides an accurate measurement of the location of initial surface contact and continuous measurement of contact stiffness as a function of penetration depth. The indenter tip was calibrated with a reference fused silica sample to determine the contact area as a function of indenter displacement into the surface.

The method proposed by Oliver and Pharr [9] was used to quantify nanoindentation hardness H and indentation modulus E. During this study, at least 150 indents were made into the samples with a target maximum indentation depth of 1500 nm. Surface position corrections were made for each indentation before data analysis. For consistency, load and contact stiffness data averaged between 1300 and 1400 nm indentation depth were used to calculate indentation hardness and elastic modulus, avoiding the depth range within which there is a strong indentation size effect.

Mechanical tests were conducted at the Fusion Materials Laboratory, KIT IAM-MMI, utilizing a universal testing machine equipped with a vacuum furnace installed inside the Hot Cell. Due to the extreme hardness of beryllides, specialized tooling made of silicon nitride was employed. The crosshead speed was adjusted to 0.05 mm/min. The sample evaluations spanned temperatures ranging from 20 to 1000°C. Miniature specimens measuring Ø2.2 × 2.6 mm were utilized for the mechanical compression tests. The reduced size of the specimens was necessary because of the machine's force limit of 10 kN and the planned future neutron irradiation and testing of the same specimens on the same equipment. To validate the data obtained from the miniature specimens, an additional set of larger specimens, measuring Ø5 × 6 mm, was manufactured and subjected to testing under specific conditions in air within the temperature range of 20–1200°C. 3-point bending tests were conducted using the same testing equipment, employing specimens sized at 27 mm × 4 mm × 3 mm. The distance between the lower rollers was set to 25 mm, and the tests were carried out across temperatures spanning 20–1000°C.

3. Results and discussion

3.1. Material selection

The selection of a suitable NMM is a key design decision in the development of breeding blanket systems for fusion power reactors, as it directly affects the neutron balance and, consequently, the tritium breeding efficiency. Among all elements, only beryllium and lead are considered viable options due to their ability to participate in (n,2 n) reactions with relatively high cross-sections, while exhibiting comparatively low (n,γ) reaction rates [3]. However, their neutronic performance diverges significantly as a function of neutron energy.

To assess their effectiveness, we analyzed the energy-dependent

neutron cross-sections for both (n,2 n) and parasitic (n,γ) reactions using evaluated nuclear data libraries (JEFF-3.3 [10] and JENDL-4.0 [11]). As shown in Fig. 2, beryllium begins to undergo (n,2 n) reactions at neutron energies around 2 MeV, enabling efficient use of moderated neutron spectra. In contrast, lead requires neutron energies near 8 MeV, which severely limits its effective multiplication window. This constraint also implies that in lead-based blankets, the use of structural materials (such as steel or tungsten) that may moderate neutrons must be minimized. This is not always feasible, particularly given that liquid lead can cause corrosion of structural steels. In summary, beryllium offers clear advantages in terms of neutron physics.

Lead's low melting point of 327°C suggests its potential use in liquid form, posing unresolved challenges related to liquid metal corrosion, magnetohydrodynamics, gas bubbles formation, and solidification of liquid metal in channels. Other lead-based materials that could be employed in solid form, such as lanthanum [12] and zirconium plumbide, are also under current consideration. Conversely, beryllium metal exhibits significant swelling under neutron irradiation and retains a considerable amount of radioactive tritium generated during this process [13,14]. This characteristic pose safety concerns and complicates its utilization and recycling processes. To mitigate these issues while retaining favorable neutronic properties, attention has turned to beryllium-based intermetallic compounds (beryllides). Results from multiple irradiation campaigns have shown that beryllides exhibit enhanced stability under neutron exposure, with reduced swelling and tritium retention [15–17].

Although beryllium forms intermetallic compounds with many metals [18], only a few satisfy the demanding requirements for application in fusion environments [3]. Firstly, the resultant beryllide should have the highest feasible tritium breeding ratio (TBR). Secondly, the second component should not produce long-lived isotopes when exposed to irradiation. Thirdly, the beryllide must withstand operational conditions within a blanket, including temperatures up to 1000°C, rapid temperature changes, and potential exposure to a corrosive environment comprising helium and hydrogen with water vapor and impurity gases.

Following an extensive screening, $TiBe_{12}$ and $CrBe_{12}$ were identified as the most promising candidates. Both compounds combine high neutronic performance with radiation stability and industrial feasibility, and neither contains elements known to produce long-lived activation products. In contrast, other candidates such as vanadium beryllide were excluded due to the toxicity of vanadium powder, which makes industrial-scale production unsafe. Zirconium beryllide ($ZrBe_{13}$) was also eliminated from consideration due to the formation of long-lived Nb isotopes upon activation of zirconium. Based on these considerations, $TiBe_{12}$ and $CrBe_{12}$ were selected for full-scale industrial fabrication in collaboration with UMP. The resulting blocks were then subjected to comprehensive microstructural and mechanical characterization, as detailed in the following sections.

3.2. General properties and microstructure

Since the successful demonstration of full-size titanium beryllide block production in 2019, titanium beryllide has emerged as the reference neutron multiplier material for the HCPB blanket design of EU DEMO [5]. The technology for manufacturing these blocks has now reached an advanced stage, with a total of 20 blocks manufactured, including 14 full-size ones. Furthermore, in 2020, UMP achieved the production of the first full-size block of chromium beryllide as a backup solution to titanium beryllide. UMP manufactured six blocks of chromium beryllide, comprising two full-sized blocks and an additional four measuring approximately Ø50 mm × 50 mm.

Fig. 3 shows a photograph of full-size beryllide blocks produced by the VHP method. These blocks are distinguished by their significant size, surpassing any beryllide blocks previously produced. The $TiBe_{12}$ block measures Ø144 × 150 mm with a central hole of Ø80 mm. The $CrBe_{12}$ block is smaller, measuring about Ø85 mm × 80 mm. It's evident that manufacturing a smaller block is a simpler task and it doesn't require perforating a hole. The technology allows the production of even larger beryllide blocks, reaching sizes up to 400 mm in diameter and height. The blocks have a metallic sheen, a characteristic feature of beryllide materials, and have visible traces of EDM.

Table 1 presents the chemical composition of the investigated beryllide blocks. These materials exhibit minimal impurity levels, except for oxygen, which is a prevalent impurity in beryllium and beryllium-based materials [18]. Notably, the exceptionally low uranium content, approximately 0.39–0.54 ppm, stands out as a significant advantage of UMP-produced beryllium. The difference in the content of nitrogen, magnesium, silicon, and calcium can be explained by the different content of these impurities in the corresponding titanium or chromium powders. Additionally, the Ti and Cr content in the blocks is lower than the stoichiometric values of 30.8 wt% and 32.5 wt%, respectively. This variation may suggest the presence of a free beryllium phase.

Table 2 presents the density values of the titanium and chromium beryllide blocks, which exceed 98 % of the corresponding theoretical densities (TD). The TD value used for $TiBe_{12}$ was 2.288 g/cm^3 and for $CrBe_{12}$ was 2.437 g/cm^3 [19]. Such density values are relatively high for

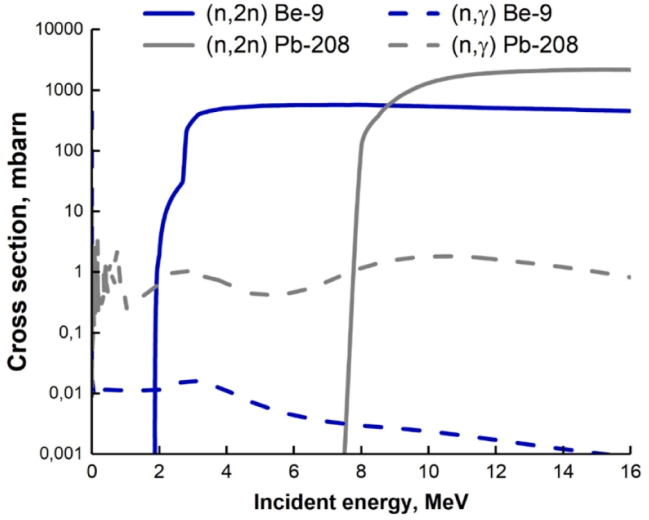

Fig. 2. Cross-section plot depicting (n,2 n) and (n,γ) reactions in relation to incident energy for Be-9 and Pb-208 [10,11].

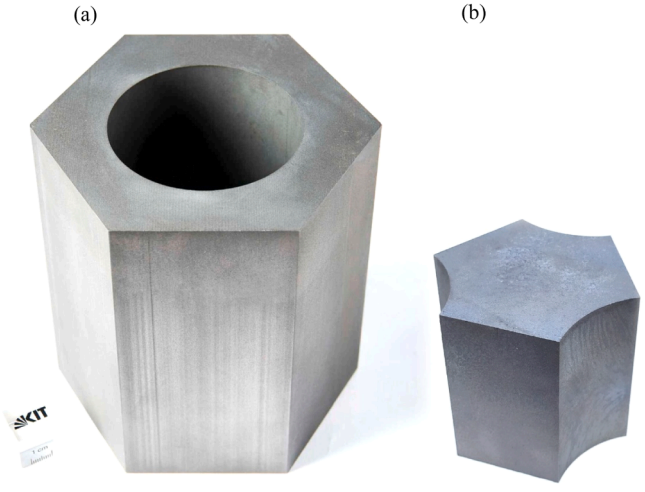

Fig. 3. Beryllide blocks manufactured at Ulba Metallurgical Plant: (a) full-size $TiBe_{12}$ block of about Ø144mm× 150 mm, (b) full-size $CrBe_{12}$ block of about Ø85mm× 80 mm.

Table 1
Chemical composition of beryllide blocks in wt%. The uranium content is presented in ppm.

Material	Ti	Cr	C	N	O	Mg	Al	Si	Ca	Fe	U, ppm	Be
$TiBe_{12}$	27.8	–	0.034	0.106	0.686	< 0.00005	0.020	0.0162	0.015	0.118	0.395	Bal.
$CrBe_{12}$	–	30.8	0.0346	0.0177	0.555	< 0.0002	0.0156	0.0237	0.0088	0.114	0.54	Bal.

Table 2
Density and volume fractions of constituent phases in blocks of titanium and chromium beryllide. TD is the theoretical density of the corresponding beryllide.

Material	Density, g/cm^3	Density, % of TD	Phase	Volume fraction, %
$TiBe_{12}$	2.25	98.3	$TiBe_{12}$	≈ 93
			Be+BeO+porosity	≈ 7
$CrBe_{12}$	2.401	98.5	$CrBe_{12}$	> 98
			Be+BeO+porosity	< 2

materials manufactured through powder metallurgy, considering that some level of porosity is typically inherent in such production methods.

The presence of the intended beryllide phases was confirmed through XRD analysis (Fig. 4). In Fig. 4a ($TiBe_{12}$), the diffraction pattern matches well with the reference data for $TiBe_{12}$, and no reflections of lower titanium beryllides (e.g., Ti_2Be_{17}, $TiBe_2$) were detected. In addition to $TiBe_{12}$, minor peaks at around 46° and 50.5° indicate the presence of a small fraction of metallic beryllium. The main Be peak at ≈ 51.5° almost coincides with one of the $TiBe_{12}$ peaks; combined with the generally low intensity of Be reflections, this makes reliable quantitative phase analysis by XRD impractical. Therefore, the phase fraction assessment was primarily based on microstructural observations, as discussed below.

In contrast, the diffraction pattern of $CrBe_{12}$ (Fig. 4b) shows only the reflections corresponding to the $CrBe_{12}$ phase, and no additional peaks from metallic beryllium or the only lower beryllide in this system, $CrBe_2$. It should also be noted that the accuracy of XRD in determining phases is typically limited to ≈ 5 %; therefore, phases with a lower volume fraction cannot be reliably quantified. Furthermore, as in all powder-processed beryllium-containing materials, small amounts of BeO are expected (in line with the measured oxygen content of 0.5–0.7 wt% in the beryllides). However, due to the low volume fraction, corresponding reflections are not visible in the XRD patterns.

The microstructure analysis presented in Fig. 5 reveals that both beryllides have homogeneous grain structures. However, the microstructure of the two beryllides is significantly different. The titanium beryllide sample (Fig. 5a) contains approximately 7 % of a metallic beryllium phase (Table 2), which appears as a distinct dark phase together with pores, since in BSE mode phases with a lower average atomic number appear darker. The pure beryllium phase arises either from an initial excess of beryllium powder beyond the amount needed to compensate for evaporation during manufacturing or from insufficient diffusion time into titanium. Pores in beryllium are typically attributed to the Kirkendall effect, as beryllium diffuses into titanium much faster than the reverse, causing a net mass transfer that leaves voids behind [20–22].

In the $CrBe_{12}$ block (Fig. 5b), relatively large polygonal grains are present, and certain grains display cracks. The origin of these cracks, whether from the cutting and grinding process, despite meticulous surface preparation, or during the VHP and subsequent cooling, remains uncertain. A metallic beryllium phase is also found in chromium beryllide, but its content is estimated to be less than 2 % (Table 2). The measured porosity in both $TiBe_{12}$ and $CrBe_{12}$ is in the range of 3–5 vol%, a characteristic commonly found in materials processed via vacuum hot pressing.

In addition, beryllium oxide particles are likely present in both beryllides in amounts of about 1 vol%, as suggested by the measured oxygen content of 0.5–0.7 wt%. However, in BSE mode the contrast between metallic beryllium, pores, and BeO particles cannot be clearly distinguished. EDS analysis of both materials presented earlier in [6] confirmed the presence of BeO, predominantly at grain boundaries and triple junctions. Since beryllium itself cannot be directly detected by EDS, the BeO particles were identified by their higher oxygen content. In addition, these BeO particles often contained increased concentrations of nitrogen in both beryllides.

EBSD analysis was employed to examine the grain size and grain boundary structure of the beryllides (Fig. 5c-d). For the titanium beryllide sample, the average grain size measures approximately 7 μm, with most grains displaying 60° twin boundaries. Detailed transmission

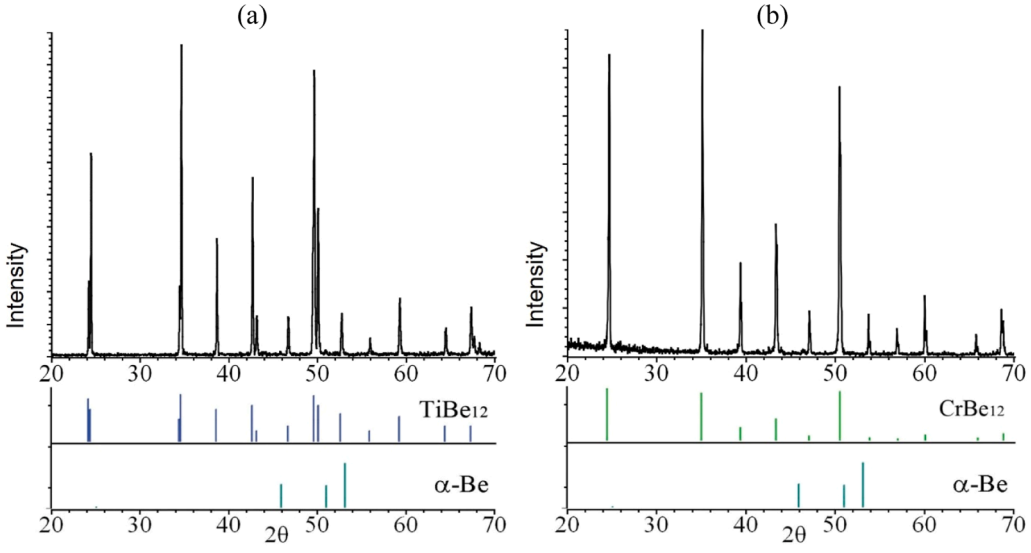

Fig. 4. X-ray diffraction patterns for (a) $TiBe_{12}$ and (b) $CrBe_{12}$ samples. Below the diffraction patterns are the peaks for the corresponding beryllides and pure Be used for the analysis.

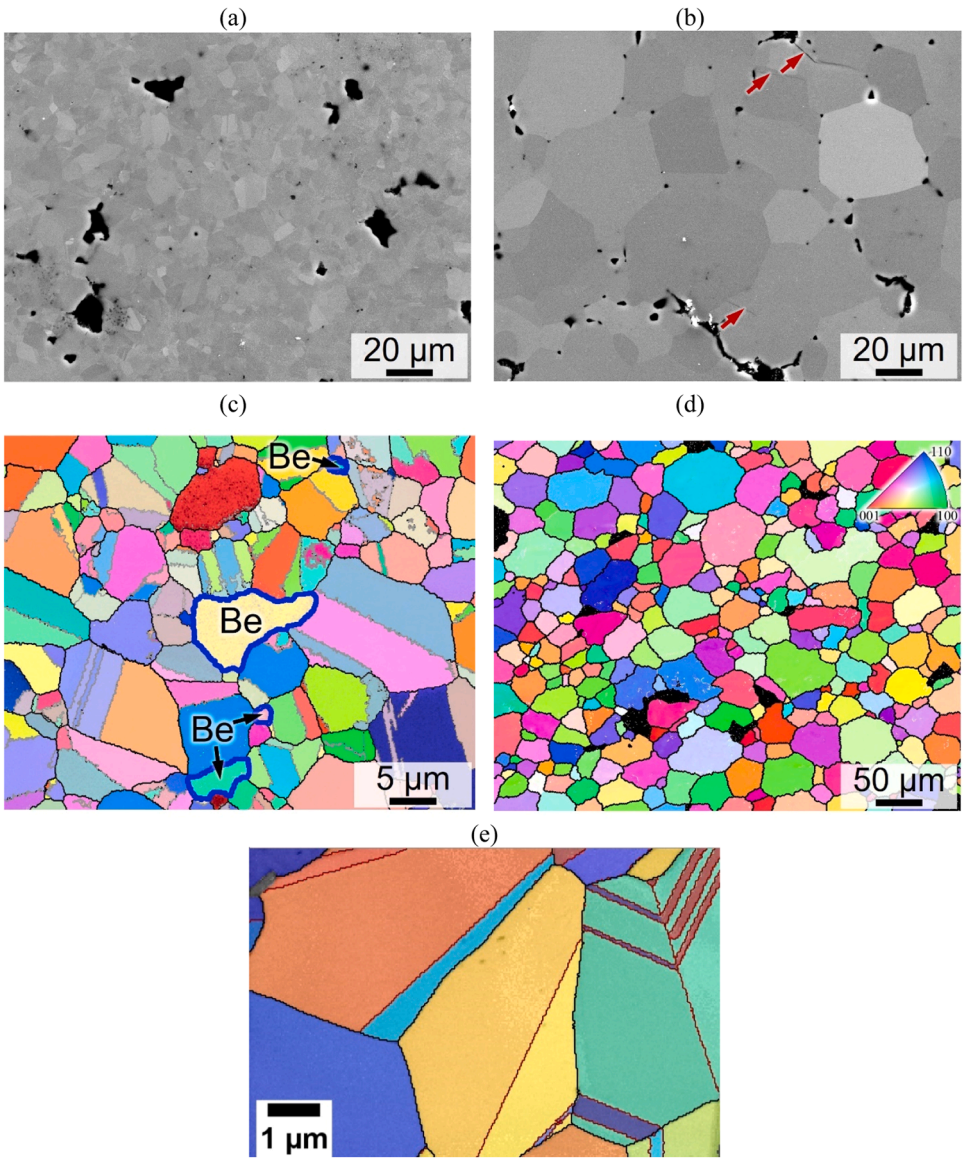

Fig. 5. (a-b) SEM microstructure in BSE mode, (c-d) EBSD and (e) TKD maps for (a,c,e) $TiBe_{12}$ and (b,d) $CrBe_{12}$. In (a,b), the metallic Be with BeO particles and pores appear as black phase. In (c), metallic Be is outlined in blue and twin boundaries in gray. The red arrows in (b) point out cracks on the surface of $CrBe_{12}$. The black areas in (d) correspond to metallic Be, BeO particles, and/or pores. In (e) grain boundaries with misorientation of 60° have red color.

Kikuchi diffraction (TKD) studies (Fig. 5e) demonstrate distribution of such twins. These twins likely formed during the hot pressing or the subsequent cooling. In contrast, the chromium beryllide sample has a coarser-grained structure, with an average grain size of around 40 μm. Notably, the larger grains of chromium beryllide show no evidence of twins. The increased grain size in the chromium beryllide can be attributed to the higher temperatures during synthesis of beryllide powder. Additionally, grain growth and the disappearance of twins may have occurred during VHP due to collective recrystallization. It's worth noting that the processing temperatures for both beryllides were the same, despite $CrBe_{12}$ having a much lower melting point than $TiBe_{12}$. Furthermore, the EBSD maps highlight the presence of metallic beryllium grains in the $TiBe_{12}$ sample (highlighted in blue) and porosity in the $CrBe_{12}$ block (black areas).

3.3. Mechanical properties

The proposed application of beryllides as functional materials within the DEMO fusion reactor blanket does not impose explicit requirements on their mechanical properties. Nonetheless, the material must uphold its structural integrity during blanket operation, avoiding excessive softening or dust formation. It should be emphasized that only very limited information on the mechanical properties of beryllides is available in the literature, mostly for $NbBe_{12}$ and Ta_2Be_{17}. This makes the mechanical behavior of beryllides rather exotic and not well explored. Therefore, the present study provides new and important data by reporting the properties of $TiBe_{12}$ and $CrBe_{12}$. The crucial factor determining beryllides' suitability for blanket use pertains to their capacity to withstand the reactor's cyclic operation, involving rapid heating to 900–1000°C followed by swift cooling to 350–400°C between cycles. Corresponding experiments are currently underway, and the outcomes will be detailed in a separate publication. This study primarily seeks to characterize beryllides, contributing to the development of a database for blanket designers.

Nanohardness testing was conducted using the Berkovich method, employing over 300 uniformly distributed test points. The test outcomes are depicted in a frequency-based nanohardness distribution diagram. Overall, nanohardness values for both materials exhibit considerable

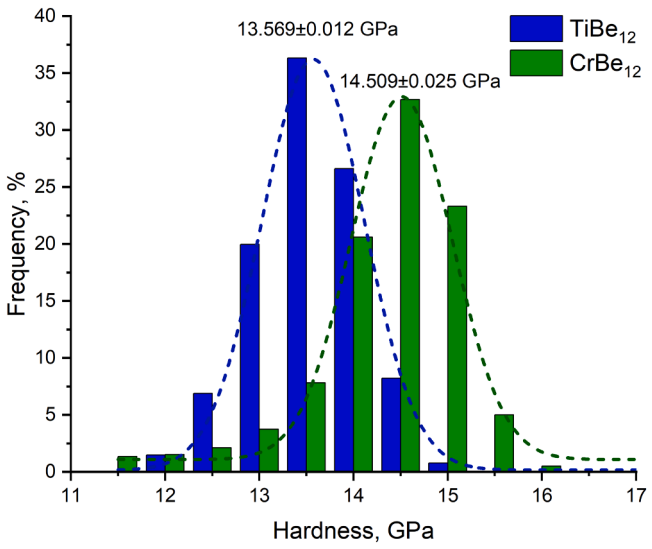

Fig. 6. Hardness distribution of titanium and chromium beryllide measured using nanoindentation. Dashed lines show Gaussian fits, with the peak hardness values indicated above the curves.

overlap. However, the peak of nanohardness for chromium beryllide measured around 14.5 GPa, whereas for titanium beryllide it reached approximately 13.6 GPa. Measured indentation elastic moduli were 304 ± 5 GPa and 285 ± 5 GPa for chromium and titanium beryllides correspondently. In a prior study [22], the peak nanohardness for titanium beryllide was established at 14.9 GPa. This result can be attributed to the notably smaller grain size of approximately 1.5–2 μm due to different manufacturing method of beryllide.

Microhardness measurements revealed values of 1010 ± 30 HV and 1030 ± 30 HV for titanium and chromium beryllide, respectively. Although chromium beryllide displayed slightly higher microhardness, the disparity is within the data scatter. Both materials exhibited remarkably high microhardness values surpassing 1000 HV, which is consistent with typical beryllide characteristics [18]. Notably, titanium beryllide, prepared by hot isostatic pressing (HIP) or spark plasma sintering (SPS), can exhibit even higher microhardness, reaching 1400–1600 HV [20,21].

Fig. 7 shows a scanning electron microscopy micrographs of indentation imprints with cracks radiating from their centers. Such behavior is characteristic of brittle materials. It's worth noting that in the case of titanium beryllide, the cracks are shorter and more numerous than in chromium beryllide. The fracture toughness, estimated by the hardness value and crack propagation distance, aligns with the prior work. The crack resistance of finer-grained titanium beryllide prepared by HIP was 2.4 ± 0.3 MPa $m^{1/2}$ at various microhardness measurement loads [20].

In this study, the crack resistance of titanium beryllide was nearly identical – 2.39 ± 0.32 MPa $m^{1/2}$, despite lower hardness and different crack lengths. Chromium beryllide exhibited significantly lower crack resistance of 0.94 ± 0.13 MPa $m^{1/2}$. This likely explains the surface cracks observed in chromium beryllide SEM images (Fig. 5b). Thus, the titanium beryllides prepared by HIP and VHP demonstrate a very similar crack resistance. Despite sharing the same crystal lattice type and similar strong covalent component in the interatomic bond, chromium beryllide exhibited significantly lower crack resistance at room temperature.

A similar surface fracture pattern around indentation prints was observed after nanoindentation, which is typical for indented brittle materials. Fig. 8a and b show representative SEM images of nanoindentation residual impressions in $TiBe_{12}$ and $CrBe_{12}$, with cracks propagating from the corners of the imprints. The images are presented at different magnifications to demonstrate the significant difference in the lengths of the indentation-induced cracks (surface fracture in chromium beryllide is significantly more developed than in titanium beryllide). It was also observed that the fracture propagation behavior differs between the two materials: while cracks in $CrBe_{12}$ are typically straight, those in $TiBe_{12}$ are segmented and frequently change direction. To gain a better understanding of the fracture behavior of these beryllides, EBSD analysis was performed on the indentation arrays. Fig. 8c and d show EBSD Euler crystal orientation maps of the investigated beryllides. In these images, dark regions indicate areas of low EBSD image quality, corresponding to grain boundaries and regions with a high density of defects.

A comparison of fracture distribution around the indentation prints revealed that while cracks in the $TiBe_{12}$ predominantly follow grain boundaries (i.e., intergranular fracture, Fig. 8c), cracks around the indents in $CrBe_{12}$ are primarily located within the grains (i.e., intragranular fracture, Fig. 8d). As described above, the grain size in $CrBe_{12}$ is nearly an order of magnitude larger than in $TiBe_{12}$. However, the intragranular nature of fracture in $CrBe_{12}$ is not solely attributed to the lower frequency of grain boundaries (GBs) around the indents. An analysis of crack distribution in $CrBe_{12}$ revealed that even when the maximum tensile stresses are expected to concentrate near GBs, only small crack segments follow the boundaries. Instead, cracks predominantly deviate from the GBs into the grain interiors (for example, see the bottom-right indent in Fig. 8c).

It was also observed that intragranular fracture propagation in the $CrBe_{12}$ intermetallic is not random but follows specific crystallographic orientations. These surface directions are highlighted by red lines in Fig. 9. This suggests that fracture occurs along specific crystallographic planes that contain the detected directions. For example, the typical fracture mechanism of beryllium involves transgranular cleavage along the basal (0001) plane [23]. Based on our observations, it is expected that $CrBe_{12}$ has more than one dominant cleavage plane. However, no literature data on the fracture crystallography of $CrBe_{12}$ are currently available. To precisely determine the fracture planes, 3D FIB/EBSD

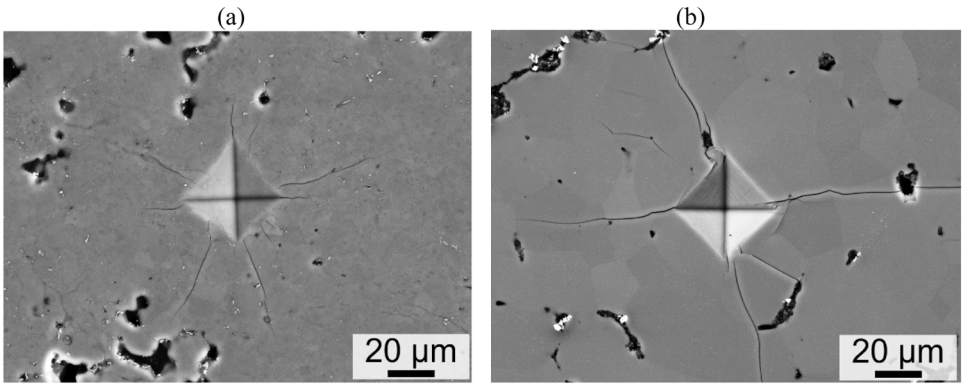

Fig. 7. SEM micrographs of indentation showing cracks in (a) $TiBe_{12}$ and (b) $CrBe_{12}$.

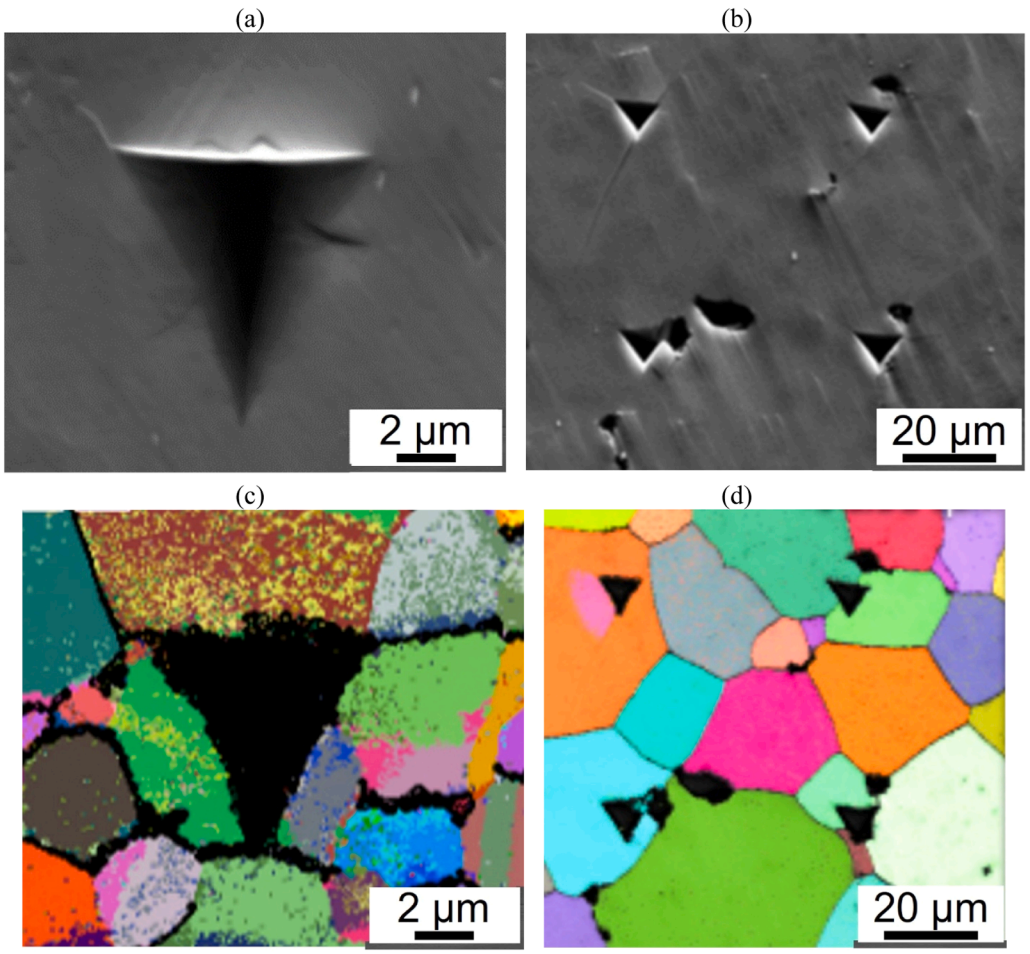

Fig. 8. SEM micrographs of residual impressions from nanoindentation hardness measurements, showing cracking in (a) $TiBe_{12}$ and (b) $CrBe_{12}$. Corresponding crystal orientation Euler maps of (c) $TiBe_{12}$ and (d) $CrBe_{12}$. In $TiBe_{12}$, cracks predominantly propagate along grain boundaries, whereas in $CrBe_{12}$, cracks around the indents are primarily intragranular.

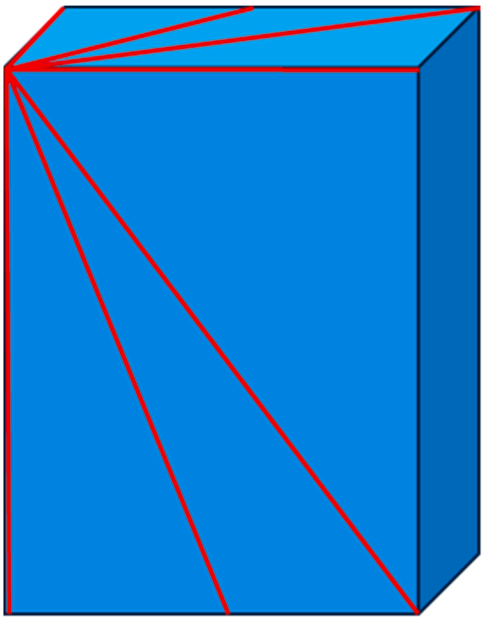

Fig. 9. Most often observed surface traces of crack segments (in red) in respect with the tetragonal lattice of $CrBe_{12}$.

analysis will be required.

Fig. 10 presents the stress-strain curves from compression tests conducted on titanium and chromium beryllides. Both materials displayed similar mechanical behavior, showcasing high strength and brittleness at room temperature, with some ductility emerging above 850°C. At room temperature, $TiBe_{12}$ exhibited a compressive strength of 2030 ± 110 MPa (Fig. 11a, Table 3). In contrast, despite its higher microhardness, $CrBe_{12}$ showed a lower compressive strength of 1750 ± 250 MPa, with a broader range of strength values, likely due to lower fracture toughness and lower ductility. Tests on larger Ø4 mm diameter specimens in air confirmed the data obtained for the smaller Ø2.2 mm diameter specimens in vacuum, with the strength of the larger specimens being only slightly lower.

As the temperature increases to 700°C, the strength of titanium beryllide gradually decreases to 1700 ± 100 MPa. Conversely, the average strength of chromium beryllide slightly increases to 1820 ± 20 MPa, although the maximum strength at this temperature is lower than at room temperature. Overall, the spread of strength values, especially for chromium beryllide, decreased, suggesting an increase in ductility. This is further indicated by the smoother bend in the stress-strain curve for titanium beryllide. Note that this material contains about 7 % of free beryllium phase that can contribute to an overall increase in ductility.

While below 800°C the strength values of two beryllides overlap, above this temperature $TiBe_{12}$ clearly exhibits higher strength than $CrBe_{12}$. At 1000°C, titanium beryllide demonstrated a strength of 740 ± 20 MPa, whereas chromium beryllide showed 460 ± 20 MPa. At

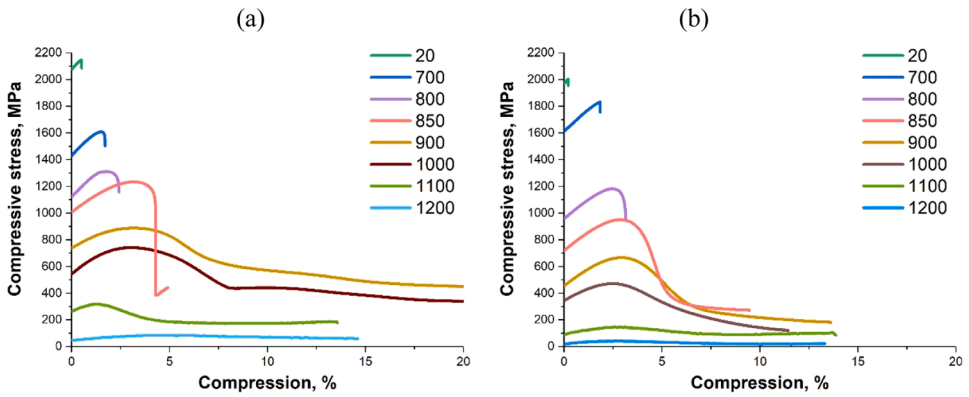

Fig. 10. Stress-strain curves in compression tests: (a) $TiBe_{12}$, (b) $CrBe_{12}$.

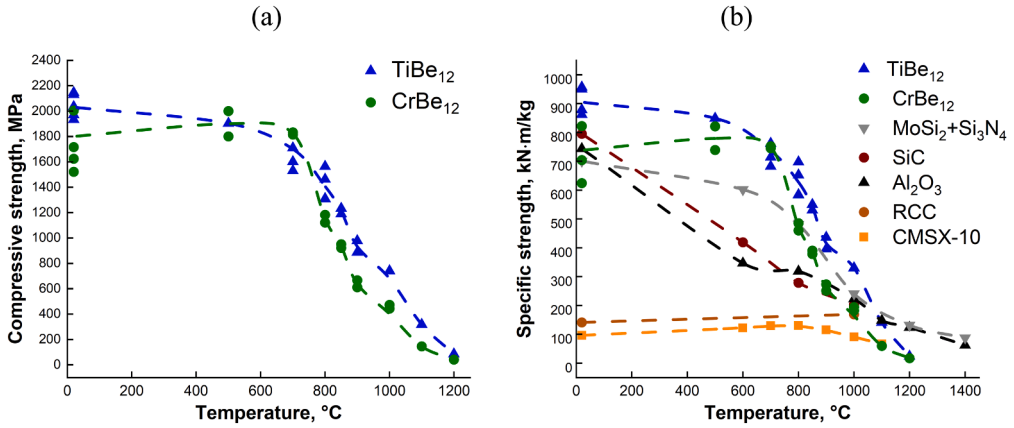

Fig. 11. (a) Compressive strength of titanium and chromium beryllides as a function of test temperature, and (b) their specific compressive strength compared to that of $MoSi_2$+Si_3N_4 [27], SiC [28], Al_2O_3 [29], as well as the specific tensile strength of reinforced carbon-carbon (RCC) [31], and the Ni-based superalloy CMSX-10 [31].

Table 3
Mechanical properties of titanium and chromium beryllides.

T, °C	Compressive strength σ_{max}, MPa		Flexural strength σ_{max}, MPa	
	$TiBe_{12}$	$CrBe_{12}$	$TiBe_{12}$	$CrBe_{12}$
20	2030 ± 110	1750 ± 250	405 ± 30	210 ± 20
400	–	–	475 ± 10	205 ± 15
500	1900 ± 100	1900 ± 140	–	–
700	1700 ± 100	1820 ± 20	460 ± 30	255 ± 30
800	1410 ± 120	1150 ± 40	500 ± 60	290 ± 5
850	1210 ± 30	940 ± 20	–	–
900	930 ± 60	640 ± 40	400 ± 15	335 ± 50
1000	740 ± 20	460 ± 20	340 ± 10	280 ± 20
1100	320 ± 15	145 ± 8	–	–
1200	85 ± 4	41 ± 2	–	–

about 850°C, beryllide samples stopped breaking down into small particles when compressed by 5 %. When the temperature increased to 900–1200°C, both titanium and chromium beryllides exhibited plastic deformation. At 1200°C, a deformation of about 20 % did not lead to the cracking of specimens. The flow stresses at this temperature were approximately 85 and 40 MPa for titanium and chromium beryllide, respectively.

Similar high-temperature compression behavior was reported for spark plasma sintered $TiBe_{12}$ by Hwang et al. [24] in the context of the JA DEMO blanket development. In their study, room-temperature compressive strength of approximately 1690 MPa was observed, gradually decreasing to 700 MPa at 1000°C. A clear yield point was first detected at 850°C, and ductility increased at higher temperatures, consistent with the onset of plastic deformation observed in our $TiBe_{12}$ samples.

In general, both beryllides exhibit similar strength values at low temperatures, despite the higher hardness of $CrBe_{12}$. However, the lower fracture toughness and presence of cracks may lead to earlier failure of $CrBe_{12}$ compared to $TiBe_{12}$. At temperatures above 800°C, chromium beryllide shows inferior strength to titanium beryllide, likely due to its lower melting point. A notable advantage of the studied materials, in comparison with ceramics, is the emergence of ductility during compression at temperatures beyond 850°C. This mechanical behavior aligns with findings in niobium beryllide, which shares the same crystal lattice type as titanium and chromium beryllide, and the decrease in strength at beyond 800°C is attributed to the initiation of plastic deformation [23]. It is shown that significant dislocation activity occurs at a temperature of 800°C, with asymmetric stacking faults attached to grain boundaries on one side, while at higher temperatures partial dislocations are observed on both sides of the stacking faults. Plastic deformation involves the activation of 1/2[101] and 1/2[100] partial dislocations, generating stacking faults on {101}, {121}, and {001} planes [26]. $NbBe_{12}$ possesses sufficient slip systems to satisfy the von Mises criterion for polycrystalline deformation at high temperatures [25,26]. Titanium and chromium beryllides are expected to exhibit similar plastic deformation characteristics and further research is planned to explore this aspect more comprehensively.

A comparison with literature data reveals that $TiBe_{12}$ exhibits remarkably high specific strength at both room and elevated temperatures (Fig. 11b). Conventional high-temperature, high-strength materials such as molybdenum silicide, aluminum oxide, and silicon carbide typically demonstrate lower compressive strength at higher densities [27–29]. Since only limited data are available on the compressive

strength of reinforced carbon-carbon and Ni-based superalloys, the specific tensile strength of these materials is shown for comparison. Even in this case, beryllides prove to be superior at least up to 1000°C. For instance, the nickel-based superalloy Inconel 718 exhibits a strength of 910 MPa at 760°C [30], whereas titanium beryllide, with 3.6 times lower density, demonstrates a strength of 1410 ± 120 MPa at 800°C. Owing to its exceptional strength-to-density ratio, titanium beryllide stands out as the material with the highest specific compressive strength within the temperature range of 20–1000°C, second only to diamond.

Three-point bending tests were conducted in a vacuum over a temperature range of 20–1000°C. While both titanium and chromium beryllide demonstrated similar mechanical behavior under compression, notable distinctions emerged during bending tests. Fig. 12a-b illustrates the flexural stress-strain curves for both beryllides. Titanium beryllide displayed only elastic behavior up to the maximum test temperature of 1000°C, with a small deflection observed at that point. In contrast, chromium beryllide exhibited elastic behavior at lower temperatures, while at 900 and 1000°C, the fracture was accompanied by notable plastic deformation. Furthermore, the flexural stress-strain curves for titanium beryllide at temperatures ranging from 400 to 800°C exhibit nearly identical profiles. In contrast, for chromium beryllide, the overall trend indicates a gradual decrease in the slope of the curves with increasing temperature.

A characteristic peak in flexural strength was observed at 800°C for $TiBe_{12}$ and 900°C for $CrBe_{12}$, which is typical for beryllides (Fig. 12c) [18,25,32,33]. Titanium beryllide consistently exhibited greater strength across all tested temperatures. At room temperature, the bending strength was 405 ± 30 MPa for titanium beryllide and 210 ± 20 MPa for chromium beryllide. This difference can be partly attributed to the different grain sizes of $TiBe_{12}$ (≈7 μm) and $CrBe_{12}$ (≈40 μm), as well as to the presence of cracks frequently observed in $CrBe_{12}$ and the higher volume fraction of free beryllium in $TiBe_{12}$. As the temperature increased, the strength of both materials also increased, reaching peak values of 540 MPa at 800°C for titanium beryllide and 370 MPa at 900°C for chromium beryllide.

In comparison to other materials, titanium beryllide exhibits significantly higher flexural strength, surpassing materials such as aluminum oxide or tantalum beryllide (up to 900°C) (Fig. 12c). Although tantalum beryllide reaches its peak flexural strength at around 1300°C, likely due to its higher melting point of 1990°C, it is noteworthy that tantalum beryllide has almost double the density (5.05 g/cm^3 [18]) of titanium beryllide. Consequently, in terms of specific flexural strength, titanium beryllide outperforms tantalum beryllide by a factor of four at temperatures ranging from 20 to 800°C. It is essential to note that for brittle materials, the flexural strength typically approaches or is slightly higher than the tensile strength. Hence, one can anticipate similar mechanical behavior in titanium and chromium beryllide during tensile tests. This alignment between flexural and tensile strength has been observed in other materials, such as niobium beryllide, where a close correspondence was reported [25].

Despite these intriguing mechanical properties, beryllides remain one of the least explored material classes, with the existing literature providing only limited information on their mechanical properties, particularly those of niobium and tantalum beryllides. The obtained data for titanium and chromium beryllides were compared with previously reported data for $NbBe_{12}$ and Ta_2Be_{17} in Fig. 13. The comparison was made using the homologous temperature T/T_m to account for differences in melting points among beryllides.

Fig. 13a illustrates the compressive strength as a function of homologous temperature for titanium, chromium, and niobium beryllides. Due to the relatively lower melting point of chromium beryllide (1338°C), the test temperatures reached up to 0.91Tm, causing the

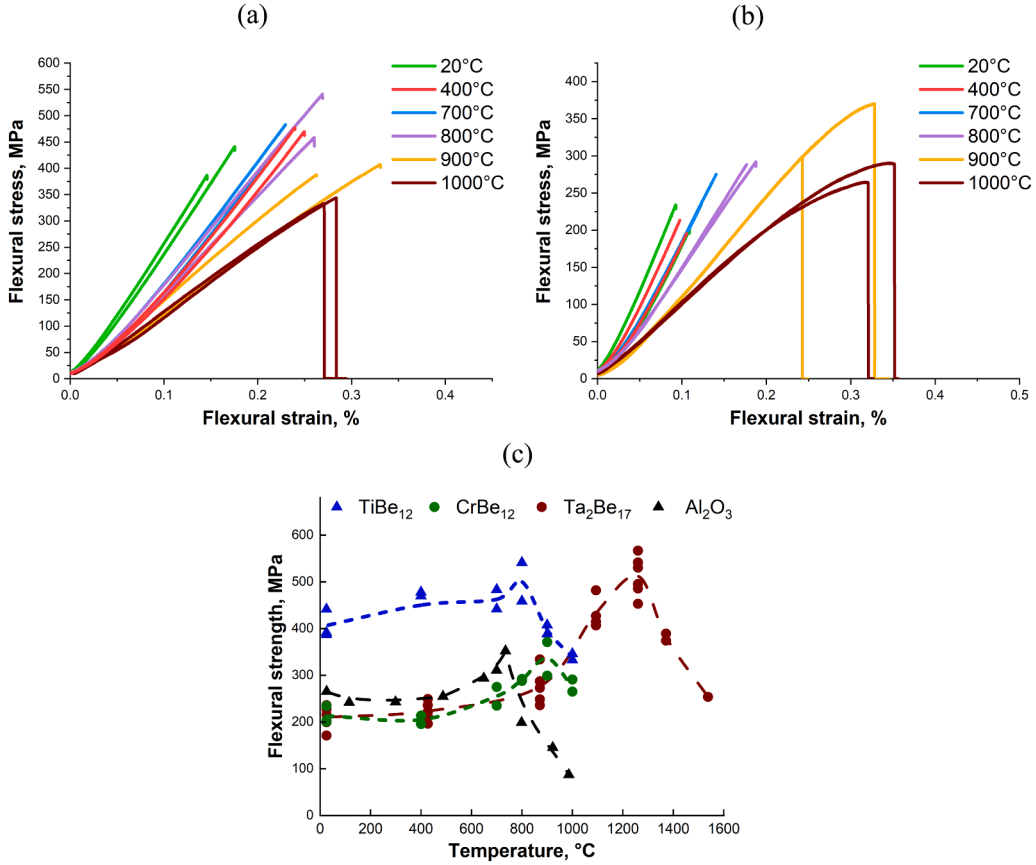

Fig. 12. Stress-strain curves from three-point bending tests for (a) $TiBe_{12}$ and (b) $CrBe_{12}$, along with their flexural strength as a function of test temperature, compared to that of Ta_2Be_{17} [18] and Al_2O_3 [34].

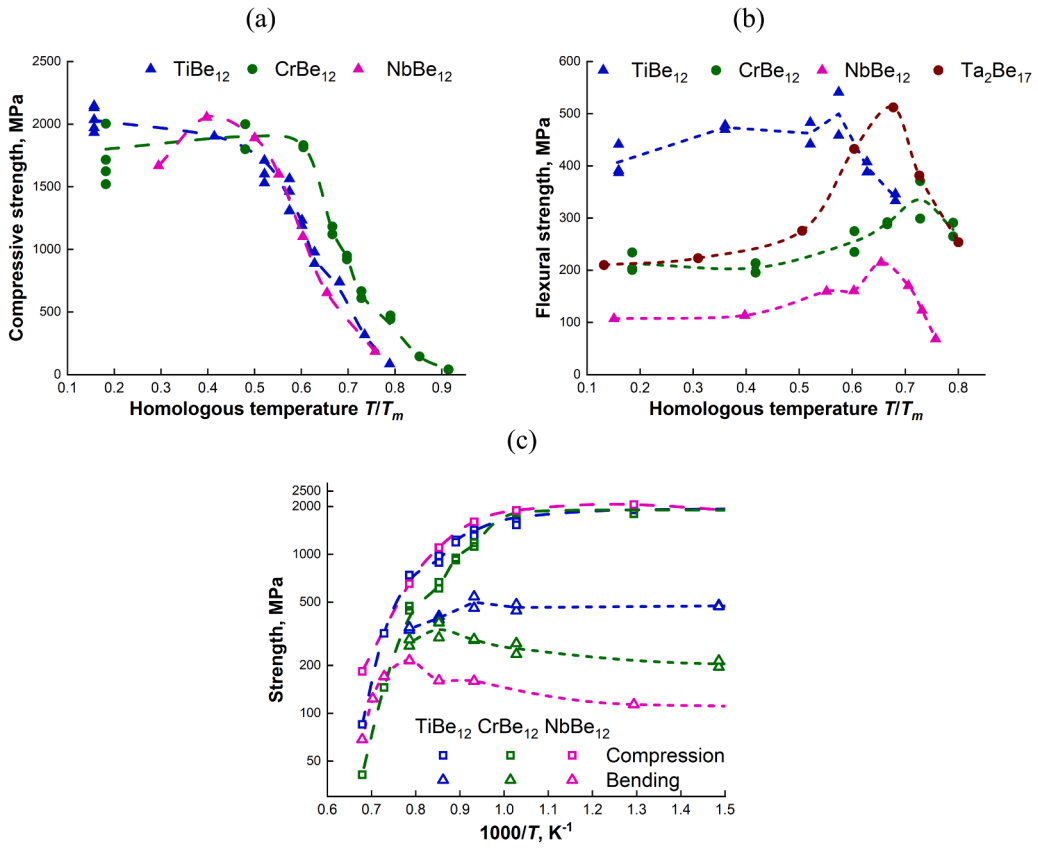

Fig. 13. Comparison of beryllide mechanical properties: (a) compressive strength and (b) flexural strength as a function of homologous temperature, and (c) compressive and flexural strength as a function of reciprocal temperature. Data for $TiBe_{12}$ and $CrBe_{12}$ are from this study, while $NbBe_{12}$ is from [25,32] and Ta_2Be_{17} from [18].

strength-temperature curve for $CrBe_{12}$ to shift towards higher temperatures compared to $TiBe_{12}$ (in contrast to Fig. 11a). Niobium beryllide, with a melting point of 1672°C, exhibits a strength trend above $0.5Tm$ similar to that of titanium beryllide, which has a slightly lower melting point of 1595°C. In the temperature range 0.3–$0.5T_m$, niobium beryllide shows a slight increase in strength, resembling the behavior observed in chromium beryllide.

Regarding the bending tests, $TiBe_{12}$ and $CrBe_{12}$ examined in this study, $NbBe_{12}$ from [25], and Ta_2Be_{17} from [18] exhibited a peak in flexural strength at high temperatures, occurring at approximately 0.55–$0.75T_m$ (Fig. 13b). Among them, titanium beryllide displayed the lowest peak temperature at $0.57T_m$. Niobium and tantalum beryllides reached their maximum flexural strength at 0.65–$0.68T_m$, while chromium beryllide exhibited a peak at an even higher homologous temperature of $0.73T_m$. Moreover, significant differences in flexural strength were observed, particularly at lower temperatures. The flexural strength was approximately 100 MPa for niobium beryllide, 200 MPa for chromium and tantalum beryllides, and 400 MPa for titanium beryllide. This variation in strength values and peak temperature can be attributed to multiple factors. For instance, titanium beryllide contains approximately 7 % of the more ductile beryllium metal phase, which may contribute to its higher flexural strength. Additionally, differences in porosity, grain size, beryllium oxide content, and other impurities may also play a role in the observed variations in flexural properties.

The evaluation of DBTT (Ductile-to-Brittle Transition Temperature) for beryllides becomes complex due to the necessity of conducting tests at high temperatures around 1000°C. However, the studies conducted in [25,32] aimed to estimate the DBTT for niobium beryllide by utilizing compression, bending, and microhardness tests. To accomplish this, the researchers established a diagram illustrating the relationship between strength and the inverse temperature of 1000/T, aiming to identify DBTT through a marked decline in strength. Fig. 13c shows that the compressive strength curve for titanium beryllide closely aligns with that of niobium beryllide, for which the estimated DBTT during compression was determined as 700–800°C [25]. However, for titanium and chromium beryllides, the DBTT during compression is more likely to be in the range of 850–900 and 800–850°C, respectively, coinciding with the appearance of notable plastic deformation on the curves.

Concerning bending tests, this study conducted assessments up to 1000°C for titanium and chromium beryllides, while niobium beryllide was tested up to 1200°C in [25]. A distinct decrease in strength was observed for niobium beryllide above 1000°C, estimating the DBTT in bending to be around 1000–1050°C. Evidently, the DBTT for titanium beryllide also seems to exceed 1000°C, despite exhibiting a lower temperature for peak bending strength compared to niobium beryllide. In the case of chromium beryllide, observable pronounced plastic deformation occurred during bending at 900–1000°C. Yet, even under these conditions, there was no significant drop in strength, suggesting that the DBTT is likely around 1000°C, but lower than the DBTT of titanium beryllide. For a more precise determination, additional bending tests at 1100 and 1200°C would be required, a capability currently unavailable with the existing equipment.

As already mentioned, the intended use of beryllides as functional materials in the breeding blanket does not impose strict mechanical property requirements on them. Nevertheless, the use of beryllides as structural materials remains highly attractive due to their exceptionally high specific strength, which is retained at elevated temperatures. As demonstrated earlier [6], beryllides can be used to fabricate components such as cones and impellers. If the challenge of limited ductility can be overcome, their application could extend to more critical structural elements subjected to bending and tensile loads, such as blades or discs for aerospace applications.

Given their high-temperature strength, beryllides are promising candidates to replace beryllium in neutron reflectors for nuclear applications, as well as in high-temperature X-ray windows. If the issue of limited ductility at ambient conditions can be resolved, their application could be extended to more demanding structural components subjected to bending and tensile loading, such as blades or discs in aerospace engineering. Even with limited ductility, beryllides may still be suitable for applications where low density and high strength are critical, such as in space technology. In this context, the development of beryllides for fusion provides a solid foundation for transferring knowledge and materials into other advanced engineering sectors.

4. Conclusions

The study represents the initiation of a comprehensive analysis of full-sized titanium and chromium beryllide blocks manufactured via vacuum hot pressing using developed industrial technology. Titanium and chromium beryllide exhibit notably distinct microstructures. Titanium beryllide has a fine grain size of approximately 7 μm with a considerable number of twins. Furthermore, the produced titanium beryllide block contains about 7 % of the free beryllium metal phase. In contrast, chromium beryllide presents coarser grains, averaging about 40 μm without any observed twins, visible cracks, and less than 2 % free beryllium. In both materials, small fractions of BeO are also present, which is typical for powder-metallurgy beryllides.

In terms of microhardness, chromium beryllide exhibits a slightly higher value, reaching 1030 HV, compared to titanium beryllide, which has a microhardness of approximately 1000 HV. Nanoindentation confirmed hardness levels of 13.6–14.5 GPa and revealed elastic moduli of 285 GPa ($TiBe_{12}$) and 304 GPa ($CrBe_{12}$). A comparison of fracture patterns around the indents revealed that intergranular fracture dominated in the $TiBe_{12}$ alloy, while $CrBe_{12}$ exhibited predominantly intragranular fracture.

The compression tests conducted at temperatures ranging from 20 to 1200°C revealed similar mechanical behaviors across the studied beryllides. Notably, at room temperature, both titanium and chromium beryllide displayed brittle fractures with substantial strengths of 2030 and 1750 MPa, respectively. However, chromium beryllide exhibited a broader scatter of strength data. With an increase in temperature up to 700°C, the strength did not change significantly. Beyond 800°C, a noticeable decrease in strength occurred. Notably, at 850°C and higher, ductility became evident in both beryllides under compression, and at 1200°C, they could be deformed by up to 20 % without developing cracks.

In the case of three-point bending tests, distinctive differences were observed between titanium and chromium beryllide, particularly in terms of strength and the temperature at which maximum flexural strength was reached. At room temperature, the bending strength was measured as 405 MPa for titanium and 210 MPa for chromium beryllide. Titanium beryllide showcased a peak flexural strength of 540 MPa at 800°C, whereas chromium beryllide demonstrated a lower maximum flexural strength of 370 MPa but at a higher temperature of 900°C. Assessing the DBTT in compression and bending revealed it to be approximately 800–900°C for compression and somewhat above 1000°C for bending.

The results are consistent with available literature on $NbBe_{12}$ and Ta_2Be_{17}, but extend the scarce mechanical database of beryllides to industrially fabricated $TiBe_{12}$ and $CrBe_{12}$. Importantly, the observed twinning in $TiBe_{12}$, combined with its fine-grained microstructure and higher specific strength, suggests a potential for enhanced toughness compared to other beryllides. Overall, this work demonstrates that $TiBe_{12}$ and $CrBe_{12}$ are not only viable neutron multiplier candidates but also possess structural properties that enable them to bridge functional and structural roles. These findings provide critical input for DEMO blanket design and broaden the applicability of beryllides to other extreme environments, including aerospace and fission systems.

CRediT authorship contribution statement

Pavel Vladimirov: Writing – review & editing, Supervision, Funding acquisition, Conceptualization. **Klaus Seemann:** Investigation. **Vladimir Chakin:** Supervision, Methodology. **Thomas Bergfeldt:** Investigation. **Rolf Rolli:** Methodology, Investigation. **Ramil Gaisin:** Writing – review & editing, Writing – original draft, Methodology, Investigation. **Viacheslav Kuksenko:** Writing – review & editing, Writing – original draft, Visualization, Methodology, Investigation. **Mikhail Podoinikov:** Writing – review & editing, Writing – original draft, Visualization, Investigation.

Declaration of Competing Interest

The authors declare the following financial interests/personal relationships which may be considered as potential competing interests. Ramil Gaisin reports financial support was provided by Euratom Research and Training Programme. If there are other authors, they declare that they have no known competing financial interests or personal relationships that could have appeared to influence the work reported in this paper.

Acknowledgements

This work has been carried out within the framework of the EUROfusion Consortium, funded by the European Union via the Euratom Research and Training Programme (Grant Agreement No 101052200 — EUROfusion). Views and opinions expressed are however those of the author(s) only and do not necessarily reflect those of the European Union or the European Commission. Neither the European Union nor the European Commission can be held responsible for them.

Viacheslav Kuksenko contribution has been funded has been part-funded by the UK EPSRC Energy Programme [grant number EP/W006839/1].

References

[1] U. Fischer, L.V. Boccaccini, F. Cismondi, M. Coleman, C. Day, Y. Hörstensmeyer, F. Moro, P. Pereslavtsev, Required, achievable and target TBR for the european DEMO, Fusion Eng. Des. 155 (2020) 111553, https://doi.org/10.1016/j.fusengdes.2020.111553.

[2] R.J. Pearson, A.B. Antoniazzi, W.J. Nuttall, Tritium supply and use: a key issue for the development of nuclear fusion energy, Fusion Eng. Des. 136 (2018) 1140–1148, https://doi.org/10.1016/j.fusengdes.2018.04.090.

[3] F.A. Hernández, P. Pereslavtsev, First principles review of options for tritium breeder and neutron multiplier materials for breeding blankets in fusion reactors, Fusion Eng. Des. 137 (2018) 243–256, https://doi.org/10.1016/j.fusengdes.2018.09.014.

[4] Y. Frants, A. Borsuk, A. Vechkutov, K. Zenkov, B. Zorin, M. Kylyshkanov, M. Podoinikov, S. Udartsev, P. Vladimirov, R. Gaisin, Titanium beryllide as an alternative to beryllium in nuclear and thermonuclear engineering, capabilities of UMP JSC in the technology development and beryllides products manufacture, J. Phys. Conf. Ser. 2155 (2022) 012015, https://doi.org/10.1088/1742-6596/2155/1/012015.

[5] R. Gaisin, V. Chakin, P. Vladimirov, F.A. Hernández, S. Udartsev, A. Vechkutov, M. Kolmakov, Industrial-scale manufacturing experience of titanium beryllide block for DEMO blanket application, Fusion Eng. Des. 161 (2020) 111862, https://doi.org/10.1016/j.fusengdes.2020.111862.

[6] R. Gaisin, Y. Frants, M. Kolmakov, B. Zorin, M. Kylyshkanov, M. Podoinikov, S. Udartsev, A. Vechkutov, V. Chakin, P. Vladimirov, Beryllium intermetallics: industrial experience on development and manufacture, Nucl. Mater. Energy 35 (2023) 101444, https://doi.org/10.1016/j.nme.2023.101444.

[7] F.A. Hernández, P. Pereslavtsev, G. Zhou, Q. Kang, S. D'Amico, H. Neuberger, L. V. Boccaccini, B. Kiss, G. Nádasi, L. Maqueda, I. Cristescu, I. Moscato, I. Ricapito, F. Cismondi, Consolidated design of the HCPB breeding blanket for the pre-Conceptual design phase of the EU DEMO and harmonization with the ITER HCPB TBM program, Fusion Eng. Des. 157 (2020) 111614, https://doi.org/10.1016/j.fusengdes.2020.111614.

[8] G. Zhou, F.A. Hernández, P. Pereslavtsev, B. Kiss, A. Retheesh, L. Maqueda, J. H. Park, The european DEMO helium cooled pebble bed breeding blanket: design status at the conclusion of the Pre-Concept design phase, Energies 16 (2023), https://doi.org/10.3390/en16145377.

[9] W.C. Oliver, G.M. Pharr, An improved technique for determining hardness and elastic modulus using load and displacement sensing indentation experiments, J. Mater. Res. 7 (1992) 1564–1583, https://doi.org/10.1557/JMR.1992.1564.

[10] OECD Nuclear Energy Agency (NEA), JEFF-3.3 Neutron Data Library, (2017). ⟨https://www.oecd-nea.org/dbdata/jeff/⟩.
[11] K. Shibata, O. Iwamoto, T. Nakagawa, N. Iwamoto, A. Ichihara, S. Kunieda, S. Chiba, K. Furutaka, N. Otuka, T. Ohsawa, T. Murata, H. Matsunobu, A. Zukeran, S. Kamada, J. Katakura, JENDL-4.0: a new library for nuclear science and engineering, J. Nucl. Sci. Technol. 48 (2011) 1–30, https://doi.org/10.1080/18811248.2011.9711675.
[12] R. Gaisin, P. Pereslavtsev, S. Baumgaertner, K. Seemann, E. Gaisina, V. Chakin, S. Udartsev, P. Vladimirov, B. Gorr, Lanthanum plumbide as a new neutron multiplier material, J. Mater. Res. Technol. 24 (2023) 3399–3412, https://doi.org/10.1016/j.jmrt.2023.03.211.
[13] V. Chakin, R. Rolli, A. Moeslang, P. Kurinskiy, P. Vladimirov, C. Dorn, I. Kupriyanov, Tritium release from advanced beryllium materials after loading by tritium/hydrogen gas mixture, Fusion Eng. Des. 107 (2016) 75–81, https://doi.org/10.1016/j.fusengdes.2016.04.018.
[14] V. Chakin, R. Rolli, R. Gaisin, P. Kurinskiy, J.-H. Kim, M. Nakamichi, Effect of heat treatment of titanium beryllide on tritium/hydrogen release, Fusion Eng. Des. 137 (2018) 165–171, https://doi.org/10.1016/j.fusengdes.2018.09.005.
[15] V. Chakin, R. Rolli, R. Gaisin, U. Hoeppener-Kramar, M. Nakamichi, M. Zmitko, Tritium release and retention in beryllium and titanium beryllide after neutron irradiation up to damage doses of 23–38 dpa, Fusion Eng. Des. 161 (2020) 111938, https://doi.org/10.1016/j.fusengdes.2020.111938.
[16] V. Chakin, A. Fedorov, R. Gaisin, M. Zmitko, Swelling of highly neutron irradiated beryllium and titanium beryllide, J. Nucl. Eng. 3 (2022) 398408, https://doi.org/10.3390/jne3040026.
[17] V. Chakin, R. Rolli, R. Gaisin, W. Van Renterghem, Tritium desorption behavior and microstructure evolution of beryllium irradiated at low temperature up to high neutron dose in BR2 reactor, JNE 4 (2023) 552–564, https://doi.org/10.3390/jne4030036.
[18] K.A. Walsh, Beryllium chemistry and processing, ASM International, 2009.
[19] G.V. Samsonov, I.M. Vinitskii, Handbook of refractory compounds (translated from the Russian by Kenneth Shaw), IFI/Plenum Press N. Y. (1980).
[20] R. Gaisin, V. Chakin, R. Rolli, J. Hoffmann, H. Leiste, T. Bergfeldt, U. Jäntsch, M. Klimenkov, J. Lorenz, A. Goraieb, P. Vladimirov, A. Möslang, Synthesis of Be12Ti compound via arc melting or hot isostatic pressing, J. Alloy. Compd. 818 (2020) 152919, https://doi.org/10.1016/j.jallcom.2019.152919.
[21] R. Gaisin, V. Chakin, M. Duerrschnabel, R. Rolli, T. Weingaertner, A. Goraieb, P. Vladimirov, Effect of HIP at 800 and 900 °C on microstructure and properties of extruded Be-Ti composites, Nucl. Mater. Energy 24 (2020) 100771, https://doi.org/10.1016/j.nme.2020.100771.
[22] R. Gaisin, V. Kuksenko, M. Duerrschnabel, V. Chakin, A. Goraieb, P. Vladimirov, Effect of HIP at 1000–1200 °C on microstructure and properties of extruded Be-Ti composites, Nucl. Mater. Energy 30 (2022) 101128, https://doi.org/10.1016/j.nme.2022.101128.
[23] D. Webster, Beryllium science and technology, Springer Verlag, 2012.
[24] T. Hwang, J.-H. Kim, Y. Sugimoto, R. Gaisin, R. Rolli, P. Vladimirov, Y. Akatsu, S. Yokohama, S. Nakano, M. Nakamichi, Effect of temperature on mechanical properties of beryllium intermetallic compounds fabricated by plasma sintering, Nucl. Mater. Energy 40 (2024) 101686, https://doi.org/10.1016/j.nme.2024.101686.
[25] C.H. Henager, S.M. Bruemmer, J.P. Hirth, Strength and toughness of beryllium niobium intermetallic compounds, Mater. Sci. Eng. A 170 (1993) 185–197.
[26] S.M. Bruemmer, L.A. Charlot, J.L. Brimhall, C.H. Henager, J.P. Hirth, Dislocation structures in be12nb after high-temperature deformation, Philos. Mag. A 65 (1992) 1083–1094, https://doi.org/10.1080/01418619208201497.
[27] M.G. Hebsur, MoSi2-Base composites, in: N.P. Bansal (Ed.), Handbook of Ceramic Composites, Springer, US, Boston, MA, 2005, pp. 173–196, https://doi.org/10.1007/0-387-23986-3_8.
[28] Adam L. McNaughton, Title: High Temperature Compression Testing of Monolithic Silicon Carbide (SiC), in: 2007.
[29] Shackelford, J.F., Alexander, W., CRC Materials Science and Engineering Handbook (3rd ed.), CRC Press., 2000.
[30] B. Geddes, H. Leon, X. Huang, Superalloys: alloying and performance, ASM International, 2010, https://doi.org/10.31399/asm.tb.sap.9781627083133.
[31] R.C. Reed, The superalloys: fundamentals and applications, Cambridge University Press, Cambridge, 2006, https://doi.org/10.1017/CBO9780511541285.
[32] C.H. Henager, R.E. Jacobson, S.M. Bruemmer, Elevated temperature mechanical properties of Be12Nb, Materials Science Engineering A 153 (1992) 416–421, https://doi.org/10.1016/0921-5093(92)90230-X.
[33] S.M. Bruemmer, J.L. Brimhall, C.H. Henager, J.P. Hirth, Properties and potential of High-Temperature niobium beryllides, MRS Online Proc. Libr. 288 (1992) 799–806, https://doi.org/10.1557/PROC-288-799.
[34] R. Morrell, National physical laboratory, handbook of properties of technical & engineering ceramics: an introduction for the engineer and designer, H.M. Stationery Office, 1985.